



28 XBAER-derived SGS and SnowEx17 measured SGS of less than 4%. The difference between
29 XBAER-derived SSA and SnowEx17 measured SSA is 2.7 m²/kg. XBAER-derived SPS can
30 be reasonable-explained by the SnowEx17 observed snow particle shapes. The comparison with
31 aircraft measurements, during the Polar Airborne Measurements and Arctic Regional Climate
32 Model Simulation Project (PAMARCMiP) campaign held in March 2018, also shows good
33 agreement (with R=0.82 and R=0.81 for SGS and SSA, respectively). XBAER-derived SGS
34 and SSA reveal the variability of the aircraft track of PAMARCMiP campaign. The comparison
35 between XBAER-derived SGS results and MODIS Snow-Covered Area and Grain size
36 (MODSCAG) product over Greenland shows similar spatial distributions. The geographic
37 distribution of XBAER-derived SPS over Greenland and the whole Arctic can be reasonable-
38 explained by campaign-based and laboratory investigations, indicating reasonable retrieval
39 accuracy of the retrieved SPS. The geographic variabilities of XBAER-derived SGS and SSA
40 over both Greenland and Arctic-wide agree with the snow metamorphism process.

41

42 **1 Introduction**

43 Change of snow properties is both a consequence and a driver of climate change (Barnett et al.,
44 2005). Snow cover and snow season, especially in Northern Hemisphere, are reported by
45 different models, to decrease due to climate change (Liston and Hiemstra, 2011). The reduction
46 of snow cover leads to the change of surface energy budget (Cohen and Rind, 1991; Henderson
47 et al., 2018), a reduction of Asian summer rainfall (Liu and Yanai, 2002; Zhang et al., 2019), a
48 loss of Arctic plant species (Phoenix, 2018) and other impacts on societies and ecosystems
49 (Bokhorst et al., 2016). Snow may influence the climate through both direct and indirect
50 feedbacks (Lemke et al., 2007). The direct feedback is the snow-albedo feedback and the
51 indirect feedbacks are involved by atmospheric circulation. The snow-albedo feedback
52 describes the mechanism that melting snow, caused by global warming, reflects less solar
53 radiation, and further enhances the warming (Thackeray and Fletcher, 2016). The snow indirect
54 feedbacks describe the impact of change snow properties on monsoonal and annular
55 atmospheric circulation (Lemke et al., 2007; Gastineau et al., 2017). However, the snow cover



56 may be declining even faster than thought due to large uncertainties of how models describe
57 the snow feedback mechanisms (Flanner et al., 2011). The uncertainties to describe the snow
58 feedback mechanisms are largely introduced by the uncertainties of knowledge of snow
59 properties (Hansen et al., 1984; Groot Zwaafink et al. 2011; Sarangi et al., 2019). Snow
60 properties depend on snow age, moisture, and temperatures surrounding (LaChapelle,1969;
61 Sokratov and Kazakov, 2012).

62 Even though model simulations and field-based *in-situ* measurements provide valuable
63 information of snow properties, such as Snow Grain Size (SGS), Snow Particle Shape (SPS),
64 Specific Surface Area (SSA) for the understanding of changing snow and its corresponding
65 impact on climate change, satellite observations offer an effective way to derive those snow
66 properties on a large scale with high quality (e.g. Painter et al., 2003; 2009; Stamnes et al., 2007;
67 Lyapustin et al., 2009; Wiebe et al., 2013). The similarities and differences of the required snow
68 parameters and their accuracy between the snow remote sensing community and other
69 communities (e.g. field-measurement community) are detailed discussed in part 1 of the
70 companion paper (Mei et al., 2020), thus we will not summery again in this paper.

71 Different retrieval algorithms to derive SGS have been developed for different instruments.
72 Airborne Visible / Infrared Imaging Spectrometer (AVIRIS) and Thematic Mapper (TM)
73 onboard Landsat are pioneer instruments used for the retrieval of SGS (Hyvarinen and
74 Lammasniemi,1987; Li et al., 2001). Painter et al. (2003,2009) retrieved SGS using AVIRIS
75 and Moderate Resolution Imaging Spectroradiometer (MODIS) data, exploring the information
76 from both visible and near-infrared spectral channels. There are several available satellite SGS
77 products for MODIS (Klein and Stroeve, 2002; Painter et al., 2009; Rittger et al., 2013) and its
78 successor, Visible Infrared Imaging Radiometer Suite (VIIRS) (Key et al., 2013). For instance,
79 the MODIS Snow-Covered Area and Grain size (MODSCAG) product is created utilizing a
80 spectral mixture analysis method based on prescribed endmember. The endmember is a
81 spectrum library for snow, vegetation, rock, and soil (Painter et al., 2009). The MODSCAG
82 algorithm can provide snow fraction and snow albedo besides SGS on a pixel base.
83 Topographic effects in MODSCAG are not considered and the MODSCAG product tends to
84 overestimate SGS (Mary et al., 2013). Other retrieval algorithms have also been designed for



85 and tested on the MODIS instrument (Stamnes et al., 2007; Aoki et al., 2007; Hori et al., 2007).
86 Jin et al (2008) retrieved SGS over the Antarctic continent using MODIS data based on an
87 atmosphere-snow coupling radiative transfer model. Lyapustin et al. (2009) proposed a fast
88 retrieval algorithm for SGS at a 1 km spatial resolution using MODIS observations. The
89 algorithm is based on an analytical asymptotic radiative transfer model. Negi and Kokhanovsky
90 (2011) proposed the usage of the Asymptotic Radiative Transfer (ART) theory to retrieve SGS.
91 The retrieved snow albedo and grain size from Negi and Kokhanovsky (2011) were validated
92 to be with good quality for clean and dry snow. However, potential problems have been reported
93 for dirty snow (e.g., soot/dust contamination). The Snow Grain Size and Pollution (SGSP)
94 algorithm retrieves SGS and pollution amount based on a snow model (Zege et al., 1998),
95 without a-priori assumptions on SPS (Zege et al., 2011). The SGSP algorithm has been
96 validated using the in-situ measurement over central Antarctica and an underestimation of
97 SGSP-derived SGS was reported under a large solar zenith angle (Zege et al., 2011; Carlsen et
98 al., 2017). The algorithm is currently implemented for the MODIS instrument and provides
99 operational daily snow products. New instruments such as Earth Observing-1 (EO-1) Hyperion
100 imagery and OLCI have also been used to derive SGS (Zhao et al., 2013; Kokhanovsky et al.,
101 2019). The algorithm proposed by Kokhanovsky et al. (2019) is conceptually based on an
102 analytical ART model, which estimates snow reflectance by given SGS and ice absorption
103 (Kokhaovksy et al., 2018). The snow grains in the ART model are described as a fractal, to
104 partly taking snow irregular shapes impacts on snow reflectance into account.

105 Snow particle shape is a fundamental parameter needed to describe snow properties
106 (Räisänen et al. 2017). The SPS keeps relatively stable before falling on the ground under cold
107 and dry conditions while it has large variabilities under warm and wet conditions (Dang et al.,
108 2016). A classification system has been proposed in Nakaya and Sekido (1938) and has been
109 updated recently by Kikuchi et al. (2013). Due to the complexity of the ice crystal shape,
110 simplified ice crystal shapes, such as fractal (Macke et al., 1996; Kokhanovsky et al., 2019) and
111 droxtal (Pirazzini et al., 2015), have been used in some satellite retrievals and model simulations.
112 However, previous investigations show that non-fractal snow types occur more frequently in
113 reality (Gordon and Taylo, 2009; Comola et al., 2017). The widely used spherical shape



114 assumption in field measurements (e.g. Flanner and Zender, 2006) is not optimal for satellite-
115 orientated retrievals, because the spherical shape assumption can not produce the angular
116 distribution of snow reflectance with required accuracy(Leroux and Fily et al., 1998; Jin et al.,
117 2008; Dumont et al., 2010), which will introduce an unacceptable magnitude of uncertainty in
118 the satellite retrieved snow properties. Details of these issues have been discussed in Part 1 of
119 the companion paper. Some attempts to derive ice crystal shape in ice clouds can be found in
120 previous publications (McFarlane et al., 2005; Cole et al., 2014). However, there is no
121 publication with respect to the retrieval of ice crystal shape in the snow layer, especially using
122 passive multi-spectrum satellite observations. Although habit mixture models are preferable for
123 the description of snow grain shapes (Saito et al., 2019; Tanikawa et al., 2020; Pohl et al., 2020),
124 the information content from satellite observation is limited compared to field-based
125 measurements. Thus, an optimal single complex shape, which provides the best agreement with
126 satellite observation (e.g. Top of the Atmosphere (TOA) reflectance) is also needed.

127 A few attempts have been proposed to retrieve SSA from space-borne observations. The
128 retrieval of SSA is actually performed based on the pre-retrieved SGS with an assumption of a
129 given known SPS. Mary et al. (2013) retrieved SSA over mountain regions using MODIS data,
130 assuming a spherical ice crystal shape. The retrieval performs a topographic correction for the
131 surface reflectance to achieve a better retrieval accuracy. The overall difference, compared to
132 field measurements, is $9.4 \text{ m}^2/\text{kg}$. Xiong et al. (2018) retrieved SSA using a snow reflectance
133 model. The model simulates the light scattering process using a Monte Carlo method and shows
134 an improvement of bidirectional reflectance, thus a better retrieval accuracy of SSA, compared
135 to the spherical assumption. The overall difference, compared to field measurements, is about
136 $6 \text{ m}^2/\text{kg}$.

137 This paper, as the companion paper of part 1, applies the XBAER algorithm on Sea and
138 Land Surface Temperature Radiometer (SLSTR) onboard Sentinel-3 to derive SGS, SPS and
139 SSA. The general concept is to use the channels, which are sensitive to SGS and SPS,
140 simultaneously. The channels used in XBAER algorithms are $0.55 \mu\text{m}$ and $1.6 \mu\text{m}$. An optimal
141 SGS and SPS pair is achieved by minimizing the difference of atmospheric-corrected
142 directional surface reflectances between satellite observations and SCIATRAN simulations.



143 SSA is then calculated based on the retrieved SGS and SPS. Nine predefined ice crystal particle
144 shapes (aggregate of 8 columns, droxtal, hollow bullet rosette, hollow column, plate, aggregate
145 of 5 plates, aggregate of 10 plates, solid bullet rosette, column) (Yang et al., 2013) are used to
146 describe the snow optical properties and to simulate the snow surface reflectance at 0.55 and
147 1.6 μm . XBAER-derived SGS, SPS, and SSA will be used to support the analysis of MOSAiC
148 (Multidisciplinary drifting Observatory for the Study of Arctic Climate) expedition
149 measurements.

150 Besides the three points we mentioned in part 1 of the companion paper, we would like to
151 emphasize one more point to avoid misunderstandings between different scientific communities.

152 ➤ **A comparison between field-measured and satellite-derived SPS.** A field-
153 measured SPS is an optical shape for a single ice crystal while satellite-derived SPS
154 is an averaged radiative shape on a certain geographic area. The geographic area is
155 determined by the instrument spatial resolution (1 kilometer as used in this study).
156 Thus it is unreasonable to directly compare a kilometer average radiative shape to a
157 single ice crystal shape. However, for a region with a similar snow metamorphism
158 process (Colbeck et al., 1980;1983), the field measured SPS may provide some
159 representative information with respect to if the ice crystal shape is convex (e.g.
160 spherical shape) or non-convex(aggregate shape), which is also critical for further
161 applications. This fundamental difference between field-measured and satellite-
162 derived SPS restricts that only a qualitative evaluation of the satellite retrieved SPS
163 is possible.

164 This paper is structured as follows: instrument characteristics of SLSTR and the *in-situ*
165 and aircraft measurements used for validation are described in section 2. Section 3 describes
166 the method including cloud screening, atmospheric correction, and the flowchart of the
167 eXtensible Bremen Aerosol/cloud and surfaceE parameters Retrieval (XBAER) algorithm.
168 Some selected data products and comparisons with MODIS products and *in-situ* data are shown
169 in section 4. The comparison with the recent campaign measurement is presented in section 5.



170 A discussion to show a time series of the retrieval results is shown in section 6. The conclusions
 171 are given in section 7.

172

173 **2 Data**

174 **2.1 SLSTR instrument**

175 After the loss of Environmental Satellite (Envisat) on 12 April 2012, the European Space
 176 Agency (ESA) launched Sentinel-3A, Sentinel-3B in February 2016, and April 2018,
 177 respectively. As the successor of Advanced Along-Track Scanning Radiometer (AATSR)
 178 onboard Envisat, Sentinel satellites take the SLSTR instrument. The SLSTR instrument has
 179 similar characteristics as compared to AATSR (see Table 1 for details). The instrument has
 180 nine spectral bands in the visible and infrared spectral range. It also has dual-view observation
 181 capability with swath widths of 1420 km and 750 km for nadir and oblique directions,
 182 respectively. The SLSTR/AATSR dual-view observations of the Earth’s surface make surface
 183 BRDF effect estimation possible, which is widely used to retrieve both surface and atmospheric
 184 geophysical parameters (Popp et al., 2016). Besides the heritage of AATSR, some new features
 185 (wider swath, new spectral bands and higher spectral resolution for certain bands) have been
 186 included in SLSTR instrument (<https://sentinel.esa.int/web/sentinel/technical-guides/sentinel-3-slstr/instrument>).
 187

188 Table 1 Instrument characteristics of AATSR and SLSTR

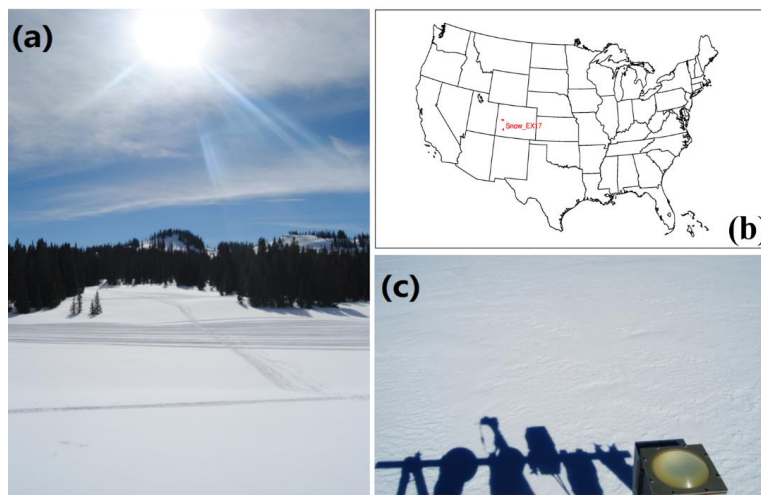
SLSTR			AATSR		
Band #	Central wavelength(μm)	Resolution(m)	Band #	Central wavelength(μm)	Resolution(m)
1	0.555	500	4	0.555	1000
2	0.659	500	5	0.659	1000
3	0.865	500	6	0.865	1000
4	1.375	500			
5	1.610	500	7	1.610	1000
6	2.25	500			
7	3.74	1000	1	3.74	1000
8	10.85	1000	2	10.85	1000
9	12	1000	3	12	1000
10	3.74	1000			
11	10.85	1000			



189 **2.2 Ground-based measurements**

190 NASA established a terrestrial hydrology program (SnowEx mission) in order to better quantify
191 the amount of water stored in snow-covered regions (Kim et al., 2017). The measurements for
192 the first year (2016 - 2017) were carried out during February 2017 (between 08 February 2017
193 and 25 February 2017) at Grand Mesa and the Senator Beck Basin in Colorado (hereafter refer
194 as SnowEx17) (See Fig. 1 (b)) (Elder et al., 2018). Grand Mesa is a forest region covered by
195 relatively homogeneous snow cover with an area size similar to airborne instrument swath
196 widths (Brucker et al., 2017) (See Fig. 1 (a)). Senator Beck Basin site has a complex topography
197 and covered by snow. The campaign used more than 30 remote sensing instruments and most
198 of the instruments are from the National Aeronautics and Space Administration (NASA) except
199 some instruments such as the European Space Agency, ESA's Radar (Kim et al., 2017). The
200 snowpits measurements provide information of snow grain size and type/shape, stratigraphy
201 profiles, and temperatures with certain information about surface conditions (e.g. snow
202 roughness) (Rutter et al., 2018). The SnowEx17 campaign provides seven different shapes
203 (New Snow, Rounds, Facets, Mixed Forms, Melt-Freeze, Crust, and Ice Lens). Table 2 lists
204 both the SnowEx17 measured snow grain shapes and SPSs defined in Yang et al. (2013). An
205 example of the snow structure/roughness can be seen from Fig. 1 (c). The measurements have
206 been publicly released in nsidc.org/data/snowex.

207



208
209



210 Fig. 1 Photos taken during the SnowEx17 campaign. (a) An overview of the campaign
 211 environment; (b) Location of SnowEx17 campaign (red rectangles); (c) A detailed example of
 212 measured snow structure/roughness (Image/photo courtesy of A. Roy, A. Langlois, and L.
 213 Brucker; supplied by the National Snow and Ice Data Center, University of Colorado, Boulder.)

214

215 Table 2 Snow grain type (shape) provided by Yang et al (2013) and *in-situ* measurements in
 216 SnowEx campaign. Please note here the grain type in Yang and measured in SnowEx17 given
 217 in the same line have not linkage

Yang			SnowEx17
Grain Type	Abbritation	Schematic drawing	Grain Type
Aggregate of 8 columns	col8e		New Snow
Droxtal	droxa		Rounds
Hollow bullet rosettes	holbr		Facets
Hollow column	holco		Mixed Forms
Plate	pla_1		Melt-Freeze
Aggregate of 5 plates	pla_5		Crust
Aggregate of 10 plates	pla_10		Ice Lens
Solid bullet rosettes	solbr		-
Column	solco		-

218

219

220

221 2.3 Aircraft observations

222 During the Polar Airborne Measurements and Arctic Regional Climate Model Simulation
 223 Project (PAMARCMiP) campaign held in March/April 2018 ground-based and airborne
 224 observations of surface, cloud and aerosol properties were performed near the Villum Research
 225 Station (North Greenland). One of the most important objectives of the PAMARCMiP 2018



226 campaign is to quantify the physical and optical properties of snow, sea ice and atmosphere
227 (Egerer, et al., 2019; Nakoudi et al., 2020). Airborne spectral irradiance measurements by the
228 Spectral Modular Airborne Radiation Measurement System (SMART) onboard the Polar 5
229 research aircraft operated by Alfred-Wegener-Institut were used to derive snow grain sizes
230 along the flight track. The SMART provides solar up- and downward spectral irradiances in the
231 range between 0.4 – 2.0 μm . The optical inlets are actively horizontally stabilized with respect
232 to aircraft movement (Wendisch et al., 2001) within 5° pitch and roll angle. In particular, for
233 high solar zenith angles (SZA) as present during PAMARCMiP (about 80° SZA) misalignment
234 of the optical inlets implies significant measurement uncertainties (Wendisch et al., 2001).
235 Further uncertainties are related to the spectral and radiometric calibration, as well as the
236 correction of the cosine response which sums up to a total wavelength-dependent uncertainty
237 (one sigma) for the irradiances ranging between 3 to 14% (Jäkel et al., 2015). The derivation of
238 the surface albedo from aircraft observations requires atmospheric corrections due to the
239 atmospheric masking by gases and molecules. There an iterative method to correct for these
240 effects was applied according to the procedure described by Wendisch et al. (2004). The
241 retrieval of the snow grain sizes is based on the method described in Carlsen et al. (2017) which
242 uses a modified approach presented by Zege et al. (2011).

243
244

245 **3 Methodology**

246 **3.1 Cloud screening**

247 The algorithm synergistically uses SLSTR and OLCI data to identify clouds over the snow
248 surface. The criteria for cloud screening over snow using SLSTR and OLCI measurements can
249 be found in Istomina et al. (2010) and Mei et al. (2017), respectively. Short summaries of
250 Istomina et al. (2010) and Mei et al. (2017) are presented below and more details can be found
251 in the original publications. The algorithm proposed by Istomina et al. (2010) for the SLSTR
252 instrument utilizes spectral behavior differences at SLSTR visible and thermal infrared
253 channels. Relative thresholds have determined based on radiative transfer simulations under
254 various atmospheric and surface conditions. The method proposed by Mei et al. (2017) for the
255 OLCI instrument uses different cloud characteristics: cloud brightness, cloud height, and cloud



256 homogeneity. The TOA reflectance at 0.412 μm , the ratio of TOA reflectance at 0.76 and 0.753
257 μm , standard deviation of TOA reflectance at 0.412 μm are used to characterize cloud
258 brightness, cloud height, and cloud homogeneity, respectively. A pixel is identified as a cloud-
259 free snow pixel when both SLSTR and OLCI identify it as a cloud-free snow pixel. Identified
260 clouds can be surrounded by a so-called “twilight zone” (Koren et al., 2007), which can extend
261 more than ten kilometers from a cloud pixel to a cloud-free area. The surrounding 5 \times 5 pixels
262 of an identified cloud pixel will be marked as a cloud to avoid the “twilight zone” effect. A
263 more details description of this cloud screening method can be found in Mei et al. (2020a).

264

265 **3.2 Atmospheric correction**

266 Due to the low atmospheric aerosol loading over the Arctic snow covered regions (e.g.
267 Greenland), atmospheric correction using path radiance representation (Chandrasekhar, 1950;
268 Kaufman et al., 1997) can provide accurate estimation of surface reflection even under
269 relatively large SZA (Lyapustin, 1999). The TOA reflectance at selected channels (0.55 and
270 1.6 μm) is described by the path radiance representation (Chandrasekhar, 1950; Kaufman et al.,
271 1997) as:

$$272 \quad R(\theta, \theta_0, \varphi, \tau, AT) = R^0(\theta, \theta_0, \varphi, \tau, AT) + \frac{T(\theta, \theta_0, \tau, AT)A}{1 - s(\tau, AT)A}, \quad (1)$$

273 where $R^0(\theta, \theta_0, \varphi, \tau, AT)$ is the TOA reflectance calculated assuming black surface (surface
274 reflectance equal 0) under VZA, SZA and RAA of $\theta, \theta_0, \varphi$. τ and AT are AOT and aerosol
275 type. $T(\theta, \theta_0, \tau, AT)$ is the total (diffuse and direct) transmittance from the sun to the surface
276 and from surface to the satellite, $s(\tau, AT)$ is spherical albedo, A is Lambertian surface albedo.

277 The atmospheric correction is performed based on the following equation:

$$278 \quad A = \frac{R(\theta, \theta_0, \varphi, \tau, AT) - R^0(\theta, \theta_0, \varphi, \tau, AT)}{(R(\theta, \theta_0, \varphi, \tau, AT) - R^0(\theta, \theta_0, \varphi, \tau, AT))s(\tau, AT) + T(\theta, \theta_0, \tau, AT)}. \quad (2)$$

279 The atmospheric correction is based on the Look-Up-Table (LUT) precalculated using
280 radiative transfer code SCIATRAN (Rozanov et al., 2014). The radiative transfer calculations



281 were performed assuming AOT values provided by MERRA simulations and aerosol type
282 defined as weakly absorbing according to our previous investigation (Mei et al., 2020b).

283

284 **3.3 XBAER Algorithm**

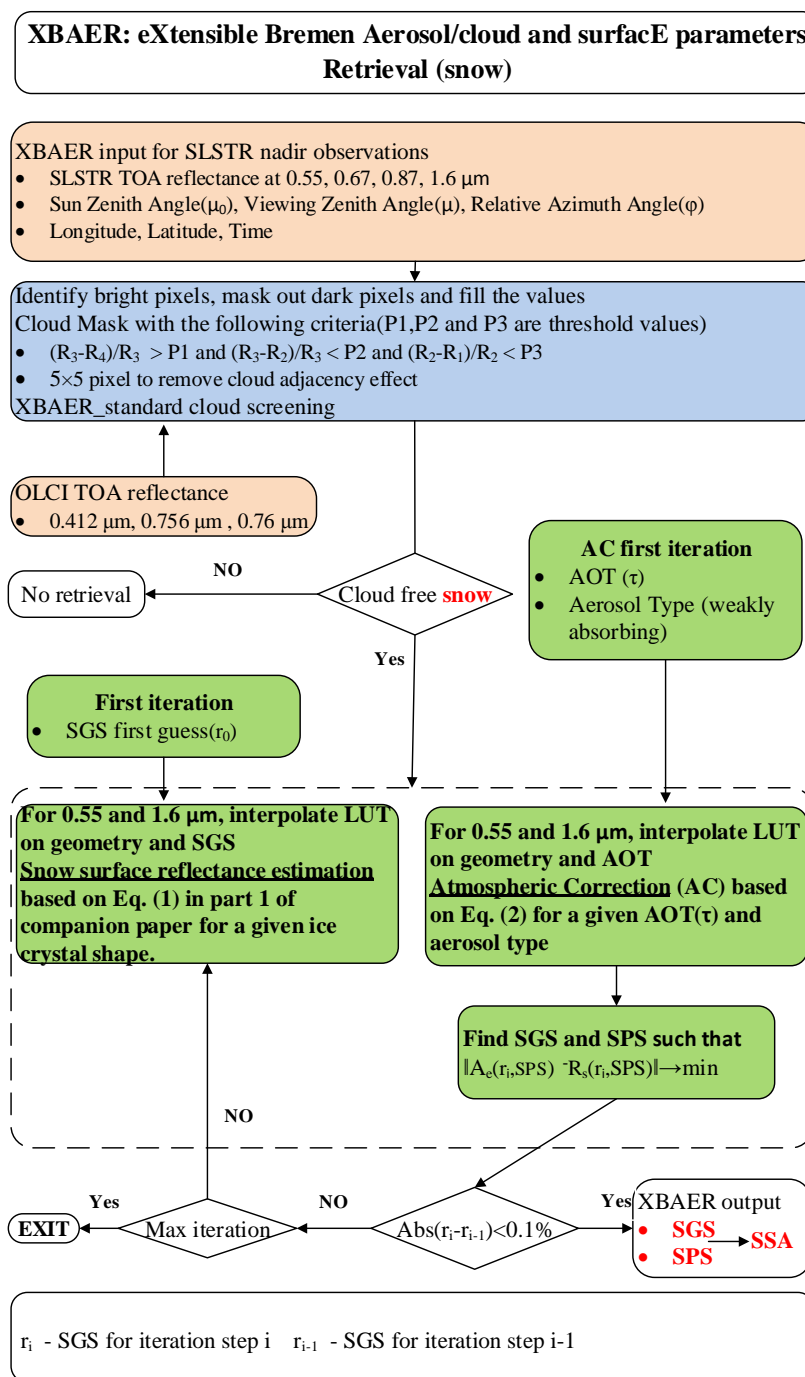
285 The theoretical background of the retrieval algorithm is given in section 4 of the companion
286 paper. The XBAER algorithm consists of three stages to derive SGS, SPS, and SSA: 1)
287 derivation of SGSs for each predefined SPS; 2) selection of the optimal SGS and SPS pairs
288 for each scenario; 3) calculation of SSA for each retrieved SGS and SPS. This section
289 describes some implementation details such as the selection of the first guess for the retrieval
290 parameters and the flowchart of the algorithm.

291 A reasonable first guess value for the iteration process can significantly reduce the
292 computation time, which is important for retrievals of atmospheric and surface properties over
293 large geographic and temporal scales with different instrument spatial resolutions. The first
294 guess of SGS in the XBAER algorithm is obtained employing the semi-analytical snow
295 reflectance model (Kokhanovsky and Zege, 2004; Kokhanovsky et al., 2018). Details of using
296 this model to derive SGS can be found in Lyapustin et al. (2009). Due to the different band
297 settings in MODIS and SLSTR (SLSTR has no 2.1 μm channel as MODIS), one non-absorption
298 channel (0.55 μm) and one absorption channel (1.6 μm) are used in our SLSTR retrieval
299 algorithm.

300 Fig. 2 shows the flowchart of how XBEAR derives SGS, SPS, and SSA. The flowchart
301 includes pre-processing of cloud screening using the synergy of OLCI and SLSTR and the
302 atmospheric correction using MERRA providing AOT and weakly absorbing aerosol type. The
303 SGS and SPS are obtained using the LUT-based minimization routine. SSA is then calculated
304 using the retrieved SGS and SPS.



305



306

307

Fig. 2 Flow chart of the XBAER retrieval algorithm



308 **4 Results**

309 Greenland is the largest ice-covered land mass in the northern hemisphere and the biggest
310 cryospheric contributor to the global sea-level rise (Ryan et al., 2019). XBAER derived SGS,
311 SPS, and SSA over Greenland enable a good understanding of the retrieval accuracy with a
312 large and representative geographic scale. Kokhanovsky et al., (2019) reported that July is an
313 optimal month to analyze satellite-derived snow properties over Greenland because Greenland
314 has a strong Snow Particle Metamorphism Process (SPMP) due to higher temperatures in July
315 (Nakamura et al. 2001). The SPMP, affected strongly by temperature, is a dominant factor for
316 the variabilities of SGS, SPS, and SSA (LaChapelle,1969; Sokratov and Kazakov, 2012; Saito
317 et al., 2019). Snow particle size increases dramatically and the ice crystal particles are
318 compacted in the strong SPMP (Aoki et al., 1999; Nakamura et al. 2001; Ishimoto et al. 2018).

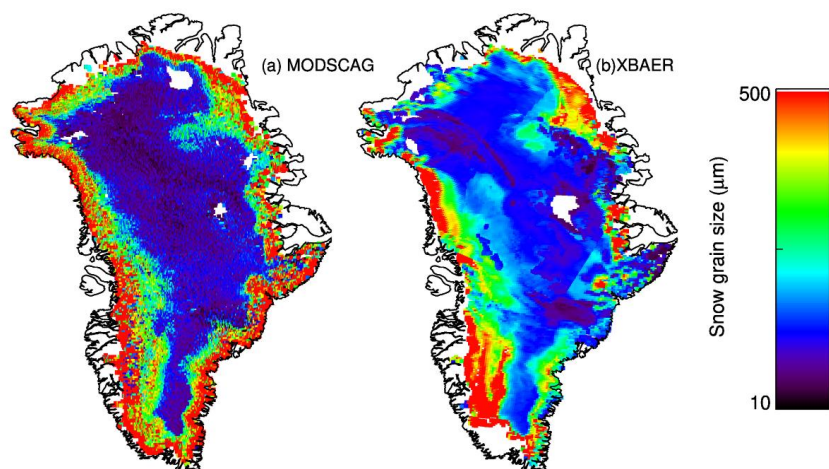
319 Fig. 3 shows an example of the XBAER-derived SGS on 28 July 2017 from SLSTR and
320 its comparison with the same scenario from MODSCAG product (Painter et al., 2009). Here
321 we chose MODIS/Aqua rather than MODIS/Terra to avoid the impact of instrument
322 degradation of MODIS/Terra (Lyapustin et al., 2014). The visualization of XBAER-derived
323 SGS is shown to be between 10 and 500 μm . The XBAER and MODSCAG derived SGS show
324 good agreement on the geographic distribution. The slight difference of cloud covered regions
325 (white parts) is explained by the different overpass time between SLSTR and MODIS. Both
326 algorithms demonstrate that SGSs in central Greenland are smaller than those at coastline
327 regions. This is attributed to the geographic distribution of surface temperature over Greenland.
328 In particular, central Greenland has a significantly higher elevation and the impacts of imperfect
329 atmospheric correction on retrieved snow properties are ignorable. The lower temperature
330 under higher elevation regions has weaker SPMP, producing more irregular SPS. The situation
331 is opposite in the coastline regions over Greenland.

332 Fig. 4 shows XBAER retrieved SGS, SPS, and SSA for 28 July 2017. Since there are no
333 available products of SPS and SSA from MODSCAG, it is a great challenge to do a similar
334 comparison as in the case of SGS. Fortunately, campaign-based and laboratory investigations
335 provide valuable information on typical snow shapes under different times/locations with a
336 wide range of atmospheric conditions (humidity, temperature, ... etc.). Kikuchi et al. (2013)

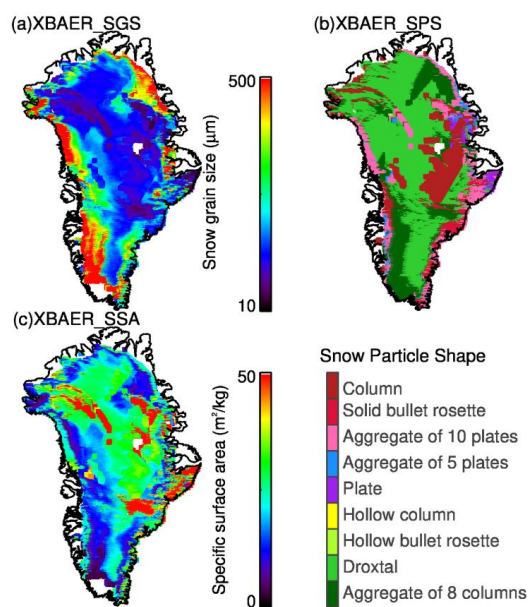


337 proposed a global classification of snow particle shape based on 21 snow/ice crystal observation
338 sites. According to Kikuchi et al. (2013), the typical SPSs in the polar regions include column
339 crystal (e.g. solid column, bullet-type crystal) with SGS of about 50 μm for solid column and
340 between 100 μm and 500 μm for bullet-type, the germ of ice crystal group with SGS of less
341 than 50 μm . Saito et al. (2019) pointed out that SPSs of fresh snow in the polar regions are
342 typically a mixture of irregular shapes such as column and platelike shape. Ishimoto et al. (2018)
343 found that aged snow can have an aggregate structure. The optical properties of small ice crystal
344 particles in aged snow may be well-characterized by granular/roundish shapes, while SPS tends
345 to be irregular or severely roughened shapes during the SPMP (Ishimoto et al., 2018). Pirazzini
346 et al (2015) investigated the impact of ice crystal sphericity on the estimation of snow albedo
347 and found droxtal is a reasonable assumption to take ice particle non-sphericity into account.
348 The above conclusions can be used as „qualitative reference“ to understand the satellite-derived
349 SPS. According to Fig. 4, central Greenland is largely covered by small particles with
350 roundish/droxtal shape while coastline regions are covered to be aggregated shapes (aggregate
351 of 8 columns, aggregate of 5 plates, the aggregate of 10 plates) with large particle sizes, are
352 essentially attributed to the different SPMP over different regions of Greenland. Bullet-type
353 crystal (solid bullet rosettes) occurred with SGS of about 100 μm . The examples shown in Fig.
354 4 can be reasonably explained by previous publications (Kikuchi et al., 2013; Pirazzini et al.,
355 2015; Ishimoto et al., 2018; Saito et al., 2019).

356 The geographic distribution of SSA is somehow anti-correlated with the geographic
357 distribution of SGS, due to the definition of SSA. Most SSA fall into the range of 10-40 m^2/kg ,
358 which agrees with previous publication (Kokhanovsk et al., 2019). The change of SSA occurs
359 especially after snowfall (Carlsen et al., 2017; Xiong et al., 2018). Since SSA contains both
360 information of SGS and SPS and field measurements provide SSA, the validation of SSA can
361 be also used as an „indirect quantitative validation“ of SPS, which will be quantitatively
362 presented in the next section.



363
364 Fig 3. A comparison of the MODISSCAG snow grain size (a) and XBAER derived snow grain
365 size (b) over Greenland on 28 July, 2017.



366
367 Fig 4. XBAER derived snow grain size and snow grain shape over Greenland for the same
368 scenario as in Fig. 3.

369
370



371 **5 Comparison and Validation**

372 In this section, we will quantitatively compare/validate XBAER derived snow properties with
373 ground-based/aircraft measurements. We emphasize that the results presented in this section is
374 considered as preliminary and the validation of our satellite-derived snow products will be
375 complemented by the MOSAiC expedition, which is now ongoing.

376 **5.1 Comparison with the observations of SnowEx17 campaign**

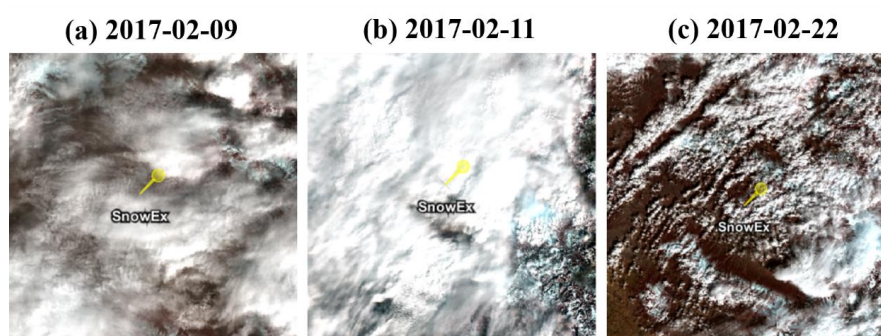
377 The above analysis shows that the XBAER is capable to derive SGS, SPS, and SSA, which
378 agrees reasonably well with existing satellite products or can be qualitatively explained by
379 campaign-based and laboratory findings. In order to have a quantitative evaluation of XBAER-
380 derived SGS, SPS, and SSA, we have collocated the SLSTR observations with recent campaign
381 measurements provided by SnowEx17, as described in section 2. Due to overpass time and
382 cloud cover, only limited match-ups between XBAER retrievals and SnowEx17 measurements
383 have been obtained.

384 Table 3 summarizes match-up information. The first three columns in Table 3 show the
385 observation time and locations (longitude and latitude). The fourth and fifth columns indicate
386 the cloud conditions. Cloud conditions in Table 3 are given by three categories: cloud-free snow,
387 cloud-contaminated snow, and cloud-covered snow. These three categories are classified by the
388 XBAER cloud identification results and are illustrated by the RGB composition figures,
389 covering the SnowEx campaign area, as presented in Fig. 4. An optically thin cloud over a
390 melting snow layer, a thick cloud over snow, and snow scenarios are presented in Fig. 4 (a), (b)
391 and (c), respectively. The cloud optical thickness (COT), estimated using the independent
392 XBAER cloud retrieval algorithm, as presented in Mei et al (2018), is ~0.5 and ~10 for 9th and
393 11th February, respectively.

394 Table 3 Information of Match-ups between SnowEx and SLSTR during February, 2017

Date	Lon(°)	Lat(°)	COT	Comment
02-09	-108.1092	39.0369	~0.5	cloud-contaminated snow
02-22	-108.0634	39.0444	0	cloud-free snow
02-22	-108.0625	39.0459	0	cloud-free snow
02-22	-108.0617	39.047	0	cloud-free snow
02-11	-108.0462	39.0278	~10	cloud-covered snow

395
396



397

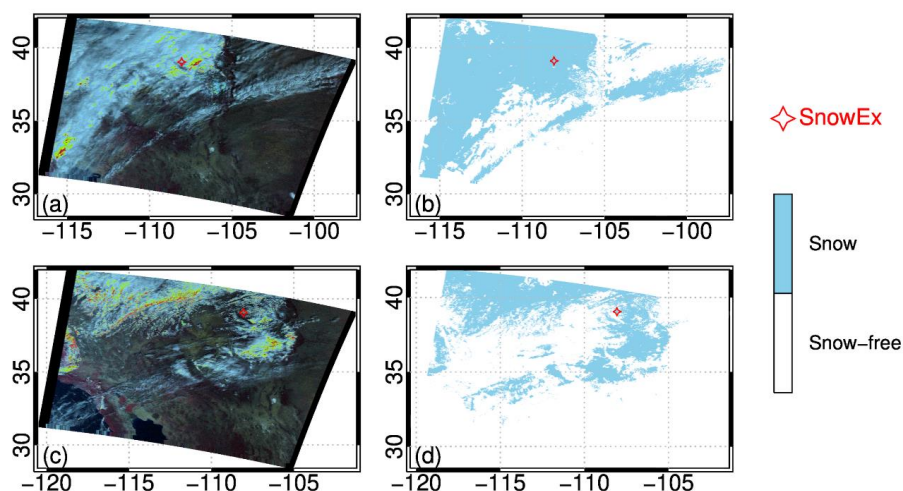
398 Fig 4. Zoom-in of the RGB composition figures (created using ESA official SLSTR software
399 SNAP) for the selected 3 days presented in Table 3. The yellow point indicate the SnowEx
400 instrument position.

401

402 Even though the synergistical use of SLSTR and OLCI provides valuable information to
403 separate cloud and snow, the identification of an optically thin cloud above a snow layer is a
404 great challenge due to the similar wavelength dependence of snow and cloud reflectance,
405 especially between snow and ice cloud (Mei et al., 2020). The identification of the cloud from
406 an underlying snow layer in XBAER relies mainly on the O₂ channel on OLCI instrument,
407 which provides the cloud height information (Mei et al., 2017). Fig. 5 shows the performance
408 of XBAER cloud identification results for cloud contamination and cloud-covered snow
409 scenarios. The red star indicates the measurement location. The zoom-in figures around the
410 measurement site is presented in Fig. 4 above. XBAER cloud screening shows, in general, a
411 good performance according to the RGB visual interpretation. However, part of the thin cirrus
412 cloud on the 9th of February is not correctly avoided. For 9th of February, XBAER cloud
413 identification give a result of clean snow while it contains a thin cloud above a snow layer. For
414 the 11th of February, XBAER has successfully detected the cloud from an underlying snow
415 layer. For a comprehensive investigation of XBAER derived snow properties under all snow-
416 cloud coupled conditions, the fifth match-up on 11th February 2017 (labeled as grey) has been
417 manually set to be „cloud free snow“. The reason to perform the validation for different cloud
418 conditions is that the satellite retrieval can only be performed under cloud-free conditions while



419 field measurements may be obtained under cloud conditions, especially when fresh snow
420 properties are measured. Thus, the field-measurements under full-cloud or partly-cloudy
421 conditions are still valuable in the validation process. According to the sensitivity study, cloud
422 contamination leads to an underestimation of SGS and the overestimation of SSA, depending
423 on the cloud fraction.



424 Fig 5. The RGB composition (left column) for 9 (a) and 22 (c) February when XBAER detect
425 as cloud free snow and provides the retrieval. The XBAER cloud screening results (right
426 column) for the corresponding days are given in (b) and (d).
427

428

429 Table 4 summarizes the comparison between XBAER retrieval results and SnowEx17
430 campaign measurements. The first three columns in Table 4 are the same as Table 3, showing
431 the observation time and locations (longitude and latitude). The second three columns are the
432 SnowEx17 measured SGS. Since the SnowEx17 provides the SGS profile up to 1 meter depth,
433 the minimum (SnowEx_min), average (SnowEx_avg), and maximum (SnowEx_max) values
434 of SGS are listed in Table 3. The last column is XBAER derived SGS. For the four cloud-filter-
435 passed match-ups, XBAER-derived SGS shows good agreement with SnowEx17
436 measurements, especially for the 22nd of February. The average absolute difference is less than
437 10 μm (4 % in relative difference). The relatively large SGS ($\geq 250\mu\text{m}$) caused mainly by the



438 warm-up on the 21st of February (see the comment in Table 5, reported by campaign
439 participators), the warmer condition leads to a quicker snow metamorphism process, forming
440 large ice crystal particles.

441 An underestimation is found for the first match-up on the 9th of February. This is explained
442 by the cirrus cloud contamination as presented in Fig. 4 and 5. According to our independent
443 XBAER cloud retrieval (Mei et al., 2018), the COT is ~0.5, cloud contamination with COT=0.5
444 introduces ~30% underestimation according to Fig. 11 in part 1 of the companion paper. So for
445 SGS=100 μm , provided by SnowEx, XBAER is expected to have a theoretically retrieved SGS
446 of ~ 70 μm while a value of 78.2 μm is obtained from the real satellite retrieval. In order to
447 further confirm this negative bias feature caused by cloud contamination, 11th February (a
448 snowstorm at the measurement site is reported by campaign participators), although filtered by
449 the XBAER cloud screening routine, is forced to retrieve the full-cloud-covered scenario as a
450 cloud-free case. According to the theoretical investigations presented in part 1 of the companion
451 paper, for $\text{COT} \geq 5$, the XBAER algorithm retrieves cloud effective radius, rather than SGS.
452 The retrieved ice crystal size depends on the cloud effective radius of the cloud above the
453 underlying snow layer. The independent XBAER cloud retrieval provides SGS value of ~ 38
454 μm while 32.3 μm is obtained by the XBAER snow retrieval, for a reference value of 100 μm
455 as provided by SnowEx17 measurement. This is consistent with a typical ice cloud effective
456 radius (King et al., 2013; Mei et al., 2018), under a snowstorm condition.

457

458 Table 4 The comparison between SnowEx SGS and XBAER retrieved SGS during February,
459 2017.

Date	Lon(°)	Lat(°)	SnowEx_min(μm)	SnowEx_avg(μm)	SnowEx_max(μm)	XBAER(μm)
02-09	-108.1092	39.0369	50	100	150	78.2
02-22	-108.0634	39.0444	100	250	500	254.4
02-22	-108.0625	39.0459	150	250	400	254.4
02-22	-108.0617	39.047	100	200	300	215.7
02-11	-108.0462	39.0278	50	100	200	32.3

460



461 Table 5 shows the same match-up information as in Table 4, but for SPS. We would like
462 to highlight again, the SPSs proposed by Yang et al (2013) are used for the radiative transfer
463 calculation. From a single ice crystal point of view, those shapes are very unlikely to occur
464 exactly in reality. This is similar to the issue in field measurements. Spherical shape assumption
465 is widely used (e.g., the measurement of SSA), however, a pure spherical shape is also very
466 unlikely to occur in natural snow. To have a reasonable comparison between satellite-derived
467 SPS and field-measured SPS, the quantitative information of „roundish“ or „irregular“ shapes
468 from both satellite and field measurement communities may be an option. Under this
469 comparison strategy, a „droxtal“ shape derived from satellite observation is somehow identical
470 with a „spherical shape“ in field measurement.

471 The second and third column in Table 5 are SnowEx17-measured and XBAER-derived
472 SPS. The abbreviations of the SPS are listed in Table 2. The 4-6th columns are the temperature,
473 wetness of snow and the comments provided by campaign, respectively. Previous publications
474 show that ice cloud and fresh snow are best described by aggregate of 8 columns (Järvinen et
475 al., 2018). Both 9th and 11th February are retrieved to be aggregate of 8 columns because both
476 of them are affected by ice cloud. The first sample on 22nd February is reported to be aggregate
477 of 8 columns and the observation of SnowEx17 is fresh snow. The SPS of the second sample
478 on 22nd February is “facet” while XBAER says “droxtal” (no exact facet shape is defined in
479 Yang et al., 2013), both tend to be roundish. It is interesting to compare the SPS for the third
480 sample on 22nd February. The SPSs are round and aggregate of 8 columns for SnowEx17
481 measurement and XBAER retrieval, respectively. The atmospheric condition is reported to be
482 “windy” and the snow layer is wind-affected and not very well-banded ice crystal. Ice crystal
483 shape in blowing snow is likely to be irregular and aggregated (Lawson et al., 2006; Fang and
484 Pomeroy, 2009; Beck et al., 2018), which is strongly affected by the near surface processes
485 (Beck et al., 2018). The wind blowing snow may be well-represented optically by a “aggregate
486 of 8 columns” shape, as retrieved by XBAER.

487

488



489 Table 5 The comparison between SnowEx snow grain shape and XBAER retrieved SGP
 490 during February, 2017.

Date	SnowEx shape	XBAER shape	Temperature (°)	Wetness	Comment
02-09	Rounds	col8e	0.2	Wet	-
02-22	New Snow	col8e	-5.1	Dry	Very surface has sparse surface hoar, affected by yesterday's warm up, bit of crust fragments
02-22	Facets	droxa	-3.6	Dry	Very very thin layer of tiny surface facets, still standing not well formed
02-22	Rounds	col8e	-1.8	Dry	Surface very wind-affected very thin (3mm) melt- freeze layer not very well-banded
02-11	New Snow	col8e	-2.5	Middle	Storm snow, some grapple, some aggregation of crystals

491

492 Table 6 shows the comparison of SSA. For the three cloud-free samples, the difference of
 493 XBAER-derived SSA and SnowEx17 measured SSA is 2.7 m²/kg, which is significantly
 494 smaller than what has been reported by previous publications. For instance, the differences
 495 between satellite retrievals and field measurements are reported to be 9 m²/kg and ~6 m²/kg as
 496 presented in Mary et al (2013) and Xiong et al (2018). An interesting case is observed for the
 497 two-sample on 22nd February (samples 3 and 4). The SGSs show the same values for these two
 498 match-ups (both are 254.4 μm from XBAER and 250 μm from SnowEx), however, ground-
 499 based measurement shows almost two times the difference of SSA (29.8 m²/kg vs 14.6 m²/kg)
 500 for these two samples, which is due to the different SPSs. SnowEx shows that the SPSs are new
 501 snow and facets for these two samples, respectively. XBAER derived SSAs are 24.5 and 12.9
 502 m²/kg, which agrees well with SnowEx measurement. Since both SnowEx and XBAER provide
 503 very similar SGS (250 μm vs 254.4 μm), the agreement of SSA indicates that XBAER derived
 504 “aggregate of 8 columns“ is comparable to „new snow“ while XBAER derived „droxtal“ is
 505 somehow „identical“ to “facets” in SnowEx. Cloud contamination introduces an overestimation
 506 of SSA, especially for 11th February. According to the investigation from the companion paper,
 507 for reference SSAs of 37.3 and 25.9 m²/kg, SSA is expected to be ~ 65 m²/kg and >100 m²/kg
 508 for cloud contamination with COT ~ 0.5 and 10, respectively. The real satellite retrieval values
 509 are 56.5 and 136.8 m²/kg, respectively.



510
511 Table 6 The comparison between SnowEx SSA and XBAER retrieved SSA during February,
512 2017.

Date	Lon(°)	Lat(°)	SnowEx(m ² /kg)	XBAER(m ² /kg)
02-09	-108.1092	39.0369	37.3	56.5
02-22	-108.0634	39.0444	18.5	17.4
02-22	-108.0625	39.0459	14.6	12.9
02-22	-108.0617	39.047	29.8	24.5
02-11	-108.0462	39.0278	25.9	136.8

513
514
515 The above validation for the retrieval of SGS, SPS, and SSA using the XBAER algorithm,
516 although with limited samples, indicate the consistent of the sensitivity study from the
517 companion paper in part 1 and the retrieval results in part 2, as presented in this section.

518
519 **5.2 Comparison with observations of aircraft campaign**

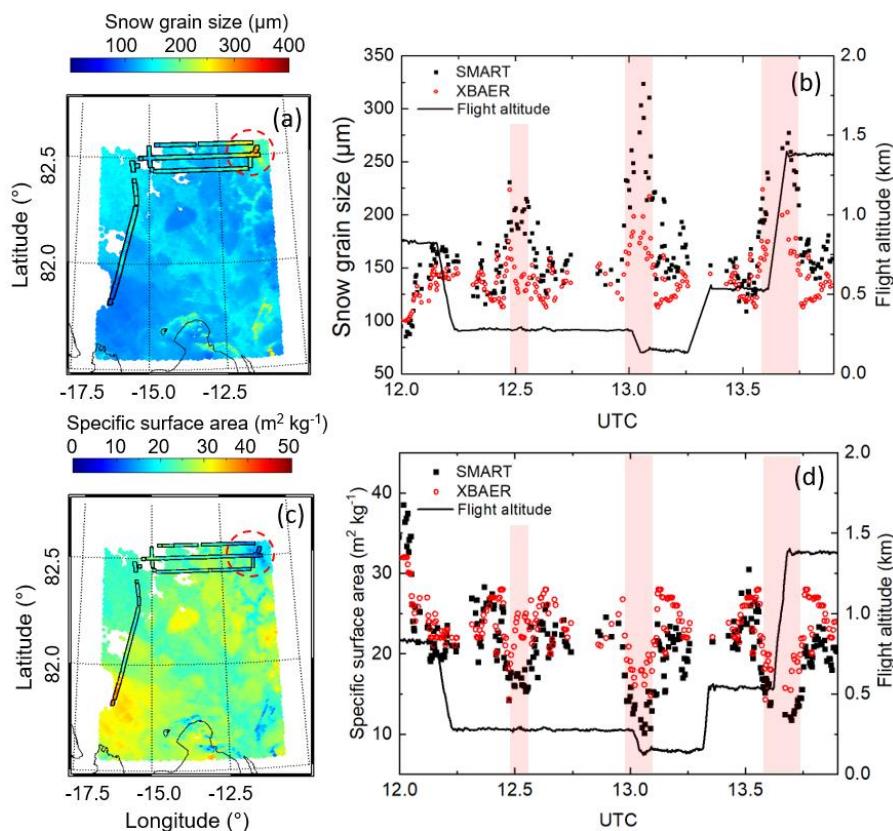
520 The optical snow grain size over Arctic sea ice was derived from airborne SMART
521 measurements as described in Sect. 2.3. Fig. 6 (a) shows the retrieved grain size along the flight
522 track (black encircled area) taken on 26 March 2018 between 12 and 14 UTC north of
523 Greenland. During this period of cloudless conditions, a Sentinel3 overpass (12:29 UTC)
524 delivered SGS data based on the XBAER algorithm as displayed in the background of this map
525 with 1 km spatial resolution. In general, lower SGS were observed by both methods in the
526 vicinity of Greenland, while in particular in the North-East region of the map (red dashed circle
527 in Fig. 6 (a)) SGS- values of up to 350 μm were derived from the aircraft albedo measurements.
528 Also the XBAER algorithm reveals higher values in this region. For a direct comparison
529 XBAER data were allocated to the time series of the SMART measurements along the flight
530 track. Afterwards all successive SMART data points assigned to the same XBAER location
531 were averaged to compile a joint time series of both data sets as displayed in Fig. 6 (b). Overall
532 a correlation coefficient of $R = 0.82$ and a root mean squared error of $\text{RMSE} = 12.4 \mu\text{m}$ was
533 derived, where SMART (mean SGS: $165 \pm 40 \mu\text{m}$) generally shows lower grain sizes than
534 XBAER (mean SGS: $138 \pm 21 \mu\text{m}$). The course of the SGS follows a similar pattern for both
535 methods, with largest deviations when the aircraft measured in the red dashed circled area from
536 Fig. 6 (a). The corresponding time periods are indicated by the light red shaded area. Camera



537 observations along the flight track have revealed an increase of surface roughness in this area.
538 Note, that the flight altitude varied for the flight section shown in Fig. 6 (a). Due to the low sun,
539 such a non-smooth surface produces a significant fraction of shadows which lowers the
540 measured albedo. Consequently, the retrieved SGS is affected in particular for the lowest flight
541 section when SMART collects the reflected radiation with high spatial resolution. This might
542 explain why the deviation of the retrieved SGS values in this area are largest around 13 UTC
543 when flight altitude was in the range of 100 m.

544 The SGS retrieval based on the algorithm suggested by Zege et al. (2011) and Carlsen et
545 al. (2017) give the optical radius of the snow grains, such that the SSA can be derived applying
546 Eq. (A1) from companion paper. The map of the SSA (Fig. 6 (c)) reflects a similar pattern than
547 observed for the SGS, showing an inverse behavior to Fig. 6 (a). In average, XBAER (mean
548 SSA: 24 ± 3 m²/kg) and SMART (mean SSA: 21 ± 5 m²/kg) agree within the 1-sigma standard
549 deviation. The correlation of SSA between XBAER and SMART is similar as for the SGS with
550 a correlation coefficient $R = 0.81$ and $RMSE = 2.0$ m²/kg.

551



552

553 Figure 6: (a) Map of SGS retrieval results from Sentinel measurements in the North of
554 Greenland from 26 March 2018. The black encircled area represent the SMART retrievals of
555 the SGS along the flight track. The red dashed circle marks a region with increased surface
556 roughness. (b) Time series of both retrieval data sets adapted to the aircraft flight path. Periods
557 matching with the circled area in (a) are shaded in light red. (c) and (d) are similar to (a) and
558 (b) but for SSA. Additionally, the flight altitude is given.

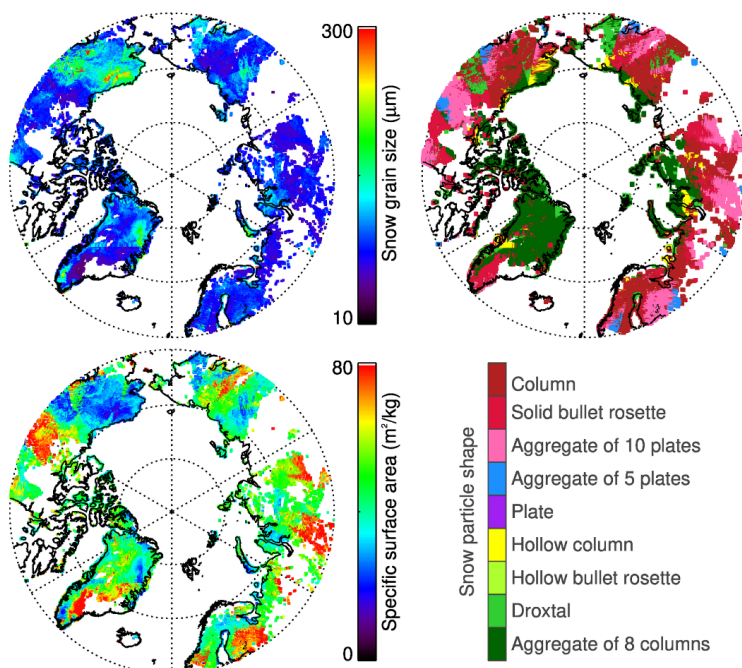
559

560 Since XBAER is also designed to support MOSAiC campaign on an Arctic-wide scale
561 (Mei et al., 2020c), it is important to have an overview of how snow properties look like on an
562 Arctic-wide scale for existing campaign. Fig. 7 shows the SGS, SPS and SSA geographic
563 distribution over the whole Arctic for 26 March 2018. Northern Greenland, North America, and
564 central Russia show large snow particles, especially over North America. And the SPS shows



565 more diversities in lower latitude compared to the central Arctic, indicating stronger SPMP. An
566 aggregated shape such as aggregate of 8 columns is the dominant shape in the central Arctic
567 while column is one of the dominant shapes in lower latitude. SSA shows large values in the
568 lower latitude Arctic (northern Canada, southern Greenland, western Norway, southern Finland,
569 northern Russia) while the values are smaller in the central Arctic.

570



571

572 Fig. 7 The distribution of XBAER-derived SGS, SPS and SSA over the whole Arctic for 26
573 March 2018

574

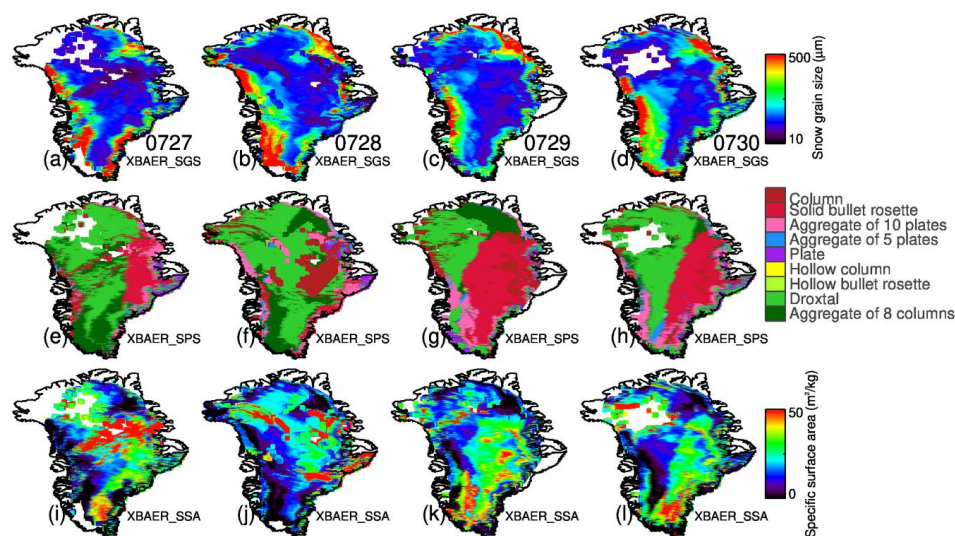
575 6 Discussion

576 The above analysis shows the promising quality of XBAER-derived SGS, SPS and SSA results.
577 The XBAER retrieved SGS, SPS and SSA can be used to understand the change of snow
578 properties temporally. Aoki et al. (2000) and Saito et al. (2019) pointed out that a 4-days time
579 scale is a reasonable time-span to see the temporal change of snow properties. Fig. 8 shows



580 XBAER-derived SGS (upper panel), SPS (middle panel) and SSA (lower panel) over
581 Greenland during 27 – 30 July, 2017. Large variability for SGS, SPS and SSA can be seen
582 during these four days, indicating the impacts of snow metamorphism on the snow properties.
583 Fig. 8 shows snow melting process in both western and northeastern parts of Greenland,
584 especially during 28 July. The strong melting in July over Greenland has also been reported by
585 Lyapustin et al (2009). SPS over southeastern part of Greenland becomes smaller during those
586 four days. No snowfall has been reported according to POLAR PORTAL report
587 (<http://polarportal.dk/en/greenland/surface-conditions/>) during these four days, thus the smaller
588 SGS may be caused by the wind-blown fresh snow, transported from central Greenland to
589 southeastern parts. This is consistent with the wind direction reported as
590 <https://www.windy.com/?62.083,2.900,4>. The change of SGS is also consistent with the change
591 of SPS. According to Fig. 8, SPSs over Greenland derived from the XBAER algorithm are
592 mainly droxtals and solid bullet rosettes for the selected days. The solid bullet rosettes and
593 droxtal are typical ice crystal shapes for fresh snow and aged snow (Nakamura et al.,2001),
594 respectively. The wind-blown fresh snow might be transported to the eastern part of Greenland,
595 and fresh snow covers the original aged snow, thus a solid bullet rosettes shape is retrieved.
596 The change of SSA follows the change of SGS and SPS. SSA over central Greenland is larger
597 while it is smaller in the coastline regions. This can be explained by the reduced SPMP impact
598 on the snow properties due to the increase of elevation in central Greenland. Inversely
599 proportional to SGS, the SSA reduces. The coverage of large SSA over the eastern part of
600 Greenland increase during these four days, indicating the „snowfall” feature due to transport.
601 This wind-induced transport feature, similar to fresh snowfall, changes both SGS and SPS. And
602 this process is revealed by and superimposed on the SPMP during the temporal change of SSA
603 retrieved from satellite observations (Carlsen et al., 2017).

604



605

606 Fig 8. XBAER derived SGS, SPS and SSA over Greenland during 27 – 30 July 2017.

607

608 7 Conclusions

609 SGS, SPS and SSA are three important parameters to describe snow properties. Both SGS, SPS
610 and SSA play important roles in the changes of snow albedo/reflectance, further impact the
611 atmospheric and energy-exchange processes. A better knowledge of SGS, SPS and SSA can
612 provide more accurate information to describe the impact of snow on Arctic amplification
613 processes. The information about SGS, SPS and SSA may also explore new applications to
614 understand the atmospheric conditions (e.g. aerosol loading). Although some previous attempts
615 (e.g. Lyapustin et al., 2009) show the capabilities of using passive remote sensing to derive
616 SGS over a large scale, no publications have been found to derive SGS, SPS and SSA
617 simultaneously. This is the first paper, to our best knowledge, attempting to retrieve both SGS,
618 SPS and SSA using passive remote sensing observations.

619 The new algorithm is designed within the framework of XBAER algorithm. The XBAER
620 algorithm has been applied to derive SGS, SPS and SSA using the newly launched SLSTR
621 instrument onboard Sentinel-3 satellite. The cloud screening is performed with a synergistical
622 technique using both OLCI and SLSTR measurements. The synergistical usage of OLCI and



623 SLSTR explore the maximum wavelength information provided by both instruments. The O₂-
624 A channel in OLCI and infrared channel in SLSTR instrument provide valuable information to
625 detect cloud over snow surfaces. The use of OLCI and SLSTR, rather than SLSTR alone, show
626 good performance of cloud screening compared to previous publications (e.g Istomina et al.,
627 2010). The synergistical cloud screening in XBAER is easy-implementable and effective-
628 runnable on a global scale, with high-quality, enables a cloud-contamination-minimized SGS,
629 SPS and SSA retrieval using passive remote sensing.

630 Besides the cloud screening, another pre-process is the atmospheric correction. Aerosol
631 plays a non-ignorable impact on the retrieval of SGS, SPS and SSA, even over the Arctic
632 regions, where aerosol loading is small (AOT, at 0.55 μ m is around 0.05) (Mei et al., 2020b). In
633 the XBAER algorithm, the MERRA simulated AOT at 0.55 μ m, together with a weakly
634 absorption aerosol type (Mei et al., 2020b) is used as the inputs for the atmospheric corrections.

635 The SGS, SPS and SSA retrieval algorithm is based on the publication by Yang et al (2013),
636 in which a database of optical properties for nine typical ice crystal shapes (aggregate of 8
637 columns, droxtal, hollow bullet rosettes, hollow column, plate, aggregate of 5 plates, aggregate
638 of 10 plates, solid bullet rosettes, column) are provided. Previous publications show that this
639 database can be used to retrieve ice crystal properties in both ice cloud and snow layer
640 (e.g., Järvinen et al., 2018; Saito et al., 2019). The algorithm is a LUT-based approach, in which
641 the minimization is achieved by the comparison between atmospheric corrected TOA
642 reflectance at 0.55 and 1.6 μ m observed by SLSTR and pre-calculated LUT under different
643 geometries and snow properties. The retrieval is relatively time-consuming because the
644 minimization has to be performed for each ice crystal shape and the optimal SGS and SPS are
645 selected after the 9 minimization are done. The SSA is then calculated using the retrieved SGS
646 and SPS based on another pre-calculated LUT.

647 The comparison between XBAER derived SGS, SPS and SSA show good agreement with
648 the SnowEx17 campaign measurements. The average absolute and relative difference between
649 XBAER derived SGS and SnowEx17 measured SGS is about 10 μ m and 4%, respectively.
650 XBAER derived SGS also shows good agreement with MODIS SGS product. XBAER



651 retrieved SPS reveals reasonable and explainable linkage with SnowEx17 measurements. The
652 difference of XBAER-derived SSA and SnowEx17 measured SSA is $2.7 \text{ m}^2/\text{kg}$. The retrieval
653 results over Greenland reveal the general patterns of snow properties over Greenland, which is
654 consistent with previous publications (Lyapustin et al. 2009). SGS is smaller over central
655 Greenland and larger over coastline regions due to the meteorological conditions. The spatial
656 distribution of SSA is somehow anti-correlated with SGS. The fresh snow and aged snow over
657 Greenland are well-captured by droxtals and solid bullet rosettes. The change of SGS, SPS and
658 SSA on a 4 days time span is also observed using XBAER retrieved SGS, SPS and SSA. The
659 comparison with aircraft measurement during PAMARCMiP campaign held in March 2018
660 also indicates good agreement ($R = 0.82$ and $R=0.81$ for SGS and SSA, respectively), XBAER-
661 derived SGS and SSA reveal the variabilities of the aircraft track of the PAMARCMiP
662 campaign. XBAER-derived SGS/SSA show smoother patterns compared to aircraft
663 measurements due to spatial resolution, height, and observation geometries. XBAER derived
664 SGS, SPS and SSA over the whole Arctic for the aircraft measurement period show strong
665 variabilities for SGS, SPS and SSA.

666 Although the presented version of the XBAER retrieval algorithm shows promising results,
667 we see at least three possibilities to improve its accuracy. An intensive validation with the
668 support of MOSAiC campaign is needed. Currently only single ice crystal shape is used in the
669 retrieval, the mixture of different ice crystal shapes i.e., the snow grain habit mixture model
670 (e.g., Saito et al. 2019) will be tested in further work. Another potential improvement may be
671 linked to the usage of polydisperse ice crystals (e.g. gamma distribution). The potential impacts
672 of the vertical structure of SGS and SPS also need to be investigated in the future.

673

674

675

676

677



678 **Acknowledgements**

679 This research was funded by the Deutsche Forschungsgemeinschaft (DFG, German Research
680 Foundation) – Project-ID 268020496 – TRR 172. The authors would like to thank Prof. Knut
681 von Salzen from Environment Canada for the valuable discussion. We thank the support from
682 Dr. Lisa Booker from National Snow and Ice Data Center, Boulder to understand the SnowEx17
683 campaign data. We thank Dr. Alexander Kokhanovsky from VITROCISET, Darmstadt,
684 Germany and Prof. Jason E. Box from Geologic Survey of Denmark and Greenland (GEUS)
685 for the valuable discussion. We thank Salguero Jaime for providing the MODSCAG snow
686 products. The MODIS snow product data are provided by MODSCAG team and SLSTR/OLCI
687 data are provided by ESA.

688
689
690
691

692 **Reference**

693 Aoki, T., Aoki, T., Fukabori, M., and Uchiyama, A.: Numerical simulation of the atmospheric effects on snow albedo
694 with a multiple scattering radiative transfer model for the atmosphere-snow system, *J. Meteor. Soc. Japan*, 77, 595–
695 614, https://doi.org/10.2151/jmsj1965.77.2_595, 1999.

696 Aoki, T., Fukabori, M., Hachikubo, A., Tachibana, Y., and Nishio, F.: Effects of snow physical parameters on
697 spectral albedo and bidirectional reflectance of snow surface, *J. Geophys. Res.*, 105(D), 10 219–10 236, 2000.

698 Aoki, T., Hori, M., Motoyoshi, H., Tanikawa, T., Hachikubo, A., Sugiura, K., Yasunari, T., Storvold, R., Eide, H.,
699 Stamnes, K., Li, W., Nieve, J., Nakajima, Y. and Takahashi, F.: ADEOS-II/GLI snow/ice products - part II:
700 Validation results using GLI and MODIS data, *Remote Sens. Environ.*, 111:274–290. doi: 10.1016/j.rse.2007.02.035,
701 2007.

702 Barnett, T. P., Adam, J. C. and Lettenmaier, D. P.: Potential impacts of a warming climate on water availability in
703 snow-dominated regions. *Nature* 438, 303–309, 2005.



- 704 Beck, A., Henneberger, J., Fugal, J. P., David, R. O., Lacher, L., and Lohmann, U.: Impact of surface and near-
705 surface processes on ice crystal concentrations measured at mountain-top research stations, *Atmos. Chem. Phys.*, 18,
706 8909–8927, <https://doi.org/10.5194/acp-18-8909-2018>, 2018.
- 707 Bokhorst, S., Pedersen, S.H., Brucker, L. et al.: Changing Arctic snow cover: A review of recent developments and
708 assessment of future needs for observations, modelling, and impacts. *Ambio*, 45, 516–537.
709 <https://doi.org/10.1007/s13280-016-0770-0>, 2016.
- 710 Brucker, L., Hiemstra, C., Marshall, H.-P., Elder, K., De Roo, R., Mousavi, M., Bliven, F., Peterson, W., Deems,
711 J., Gadomski, P., Gelvin, A., Spaete, L., Barnhart, T., Brandt, T., Burkhart, J., Crawford, C., Dutta, T., Erikstrod, H.,
712 Glenn, N., Hale, K., Holben, B., Houser, P., Jennings, K., Kelly, R., Kraft, J., Langlois, A., McGrath, D., Merriman,
713 C., Molotch, N. and Nolin, A.: A first overview of SnowEx ground-based remote sensing activities during the winter
714 2016–2017, *2017 IEEE International Geoscience and Remote Sensing Symposium (IGARSS)*, 1391-1394, doi:
715 10.1109/IGARSS.2017.8127223, 2017.
- 716 Chandrasekhar, S.: *Raditive Transfer*. London: Oxford University Press, 1950
- 717 Carlsen, T., Birnbaum, G., Ehrlich, A., Freitag, J., Heygster, G., Istomina, L., Kipfstuhl, S., Orsi, A., Schäfer, M.,
718 and Wendisch, M.: Comparison of different methods to retrieve optical-equivalent snow grain size in central
719 Antarctica, *The Cryosphere*, 11, 2727–2741, <https://doi.org/10.5194/tc-11-2727-2017>, 2017.
- 720 Colbeck, S. C.: Thermodynamics of snow metamorphism due to variations in curvature, *J. Glaciol.*, 26, 291-301,
721 10.3189/S0022143000010832, 1980.
- 722 Colbeck, S. C.: Theory of metamorphism of dry snow, *J. Geophys. Res.*, 88, 5475-5482, 1983.
- 723 Cohen, J., and D. Rind: The Effect of Snow Cover on the Climate. *J. Climate*, 4, 689–
724 706, [https://doi.org/10.1175/1520-0442\(1991\)004<0689:TEOSCO>2.0.CO;2](https://doi.org/10.1175/1520-0442(1991)004<0689:TEOSCO>2.0.CO;2), 1991
- 725 Cole, B. H., Yang, P., Baum, B. A., Riedi, J., and C.-Labonnote, L.: Ice particle habit and surface roughness derived
726 from PARASOL polarization measurements, *Atmos. Chem. Phys.*, 14, 3739-3750, [https://doi.org/10.5194/acp-14-](https://doi.org/10.5194/acp-14-3739-2014)
727 3739-2014, 2014.
- 728 Comola, F., Kok, J. F., Gaume, J., Paterna, E., and Lehning, M.: Fragmentation of wind-blown snow crystals,
729 *Geophys. Res. Lett.*, 44, 4195–4203, <https://doi.org/10.1002/2017GL073039>, 2017GL073039, 2017.



- 730 Dang, C., Fu, Q., and Warren, S. G.: Effect of snow grain shape on snow albedo, *J. Atmos. Sci.*, 73, 3573–3583,
731 <https://doi.org/10.1175/JAS-D-15-0276.1>, 2016.
- 732 Dumont, M., Brissaud, O., Picard, G., Schmitt, B., Gallet, J.-C., and Arnaud, Y.: High-accuracy measurements of
733 snow Bidirectional Reflectance Distribution Function at visible and NIR wavelengths – comparison with modelling
734 results, *Atmos. Chem. Phys.*, 10, 2507–2520, <https://doi.org/10.5194/acp-10-2507-2010>, 2010.
- 735 Egerer, U., Gottschalk, M., Siebert, H., Ehrlich, A., and Wendisch, M.: The new BELUGA setup for collocated
736 turbulence and radiation measurements using a tethered balloon: first applications in the cloudy Arctic boundary
737 layer, *Atmos. Meas. Tech.*, 12, 4019–4038, <https://doi.org/10.5194/amt-12-4019-2019>, 2019.
- 738 Elder, K., L. Brucker, C. Hiemstra, and H. Marshall. : *SnowEx17 Community Snow Pit Measurements, Version 1.*
739 [Indicate subset used]. Boulder, Colorado USA. NASA National Snow and Ice Data Center Distributed Active
740 Archive Center. doi: <https://doi.org/10.5067/Q0310G1XULZS>. [Date Accessed], 2018.
- 741 Fang, X. and Pomeroy, J. W.: Modelling blowing snow redistribution to Prairie wetlands, *Hydrol. Process.*, 23,
742 2557–2569, doi:10.1002/hyp.7348, 2009.
- 743 Flanner, M. G. and Zender, C. S.: Linking snowpack microphysics and albedo evolution, *J. Geophys. Res.*, 111,
744 D12208, doi:10.1029/2005JD006834, 2006.
- 745 Flanner, M., Shell, K., Barlage, M. et al.: Radiative forcing and albedo feedback from the Northern Hemisphere
746 cryosphere between 1979 and 2008. *Nature Geosci.*, 4, 151–155, <https://doi.org/10.1038/ngeo1062>, 2011.
- 747 Gastineau, G., J. García-Serrano, and C. Frankignoul: The Influence of Autumnal Eurasian Snow Cover on Climate
748 and Its Link with Arctic Sea Ice Cover. *J. Climate*, 30, 7599–7619, <https://doi.org/10.1175/JCLI-D-16-0623.1>, 2017.
- 749 Groot Zwaafink, C. D., Löwe, H., Mott, R., Bavay, M., and Lehning, M.: Drifting snow sublimation: A high-
750 resolution 3-D model with temperature and moisture feedbacks. *Journal of Geophysical Research*,
751 116(D16). doi:10.1029/2011jd015754, 2011.
- 752 Gordon, M. and Taylor, P. A.: The Electric Field During Blowing Snow Events, *Bound-lay. Meteorol.*, 130, 97–115,
753 2009.



- 754 Hansen J., Lacis, A., Rind D., Russel G., Stone P., Fung I., Ruedy R., Lerner J.: Climate sensitivity: analysis of
755 feedback mechanisms. *Clim. Process. Clim. Sensit.* (AGU Geophys. Monogr. Ser. 29) 5, 130–163, 1984.
- 756 Henderson, G.R., Peings, Y., Furtado, J.C. et al.: Snow–atmosphere coupling in the Northern Hemisphere. *Nature*
757 *Clim Change*, 8, 954–963, <https://doi.org/10.1038/s41558-018-0295-6>, 2018.
- 758 Hori, M., Aoki, T., Stamnes, K. and Li, W.: ADEOS-II/GLI snow/ice products - part III:retrieved results, *Remote*
759 *Sens. Environ.*, 111:291–336. doi: 10.1016/j.rse.2007.01.025, 2007.
- 760 Hyvarinen, T. and Lammasniemi, J.: Infrared measurement of free–water content and grain size of snow, *Opt.*
761 *Eng.*, 26(4), 342–348, 1987.
- 762 Ishimoto, H., Adachi, S., Yamaguchi, S., Tanikawa, T., Aoki, T. and Masuda, K. : Snow particles extracted from X-
763 ray computed microtomography imagery and their single-scattering properties, *J. Quant. Spectrosc. Radiat. Transfer*,
764 209, 113–128, <https://doi.org/10.1016/j.jqsrt.2018.01.021>, 2018.
- 765 Istomina, L. G., von Hoyningen-Huene, W., Kokhanovsky, A. A., and Burrows, J. P.: The detection of cloud-free
766 snow-covered areas using AATSR measurements, *Atmos. Meas. Tech.*, 3, 1005–1017, [https://doi.org/10.5194/amt-](https://doi.org/10.5194/amt-3-1005-2010)
767 3-1005-2010, 2010.
- 768 Järvinen, E., Jourdan, O., Neubauer, D., Yao, B., Liu, C., Andreae, M. O., Lohmann, U., Wendisch, M., McFarquhar,
769 G. M., Leisner, T., and Schnaiter, M.: Additional global climate cooling by clouds due to ice crystal complexity,
770 *Atmos. Chem. Phys.*, 18, 15767–15781, <https://doi.org/10.5194/acp-18-15767-2018>, 2018.
- 771 Jäkel, E., Mey, B., Levy, R., Gu, X., Yu, T., Li, Z., Althausen, D., Heese, B., and Wendisch, M.: Adaption of the
772 MODIS aerosol retrieval algorithm using airborne spectral surface reflectance measurements over urban areas: a
773 case study, *Atmos. Meas. Tech.*, 8, 5237–5249, <https://doi.org/10.5194/amt-8-5237-2015>, 2015.
- 774 Jin, Z., Charlock, T. P., Yang, P., Xie, Y., and Miller, W. : Snow optical properties for different particle shapes with
775 application to snow grain size retrieval and MODIS/CERES radiance comparison over Antarctica. *Remote Sensing*
776 *of Environment*, 112(9), 3563–3581. doi:10.1016/j.rse.2008.04.011,2008
- 777 Kaufman, Y. J., Tanre, D., Remer, L. A., Vermote, E. F., Chu, A., and Holben, B. N.: Operational remote sensing
778 of tropospheric aerosol over land from EOS moderate resolution imaging spectroradiometer. *Journal of Geophysical*
779 *Research: Atmospheres*, 102(D14), 17051-17067, doi: 10.1029/96JD03988, 1997.



- 780 Key, J., Mahoney, R., Liu, Y., Romanov, P., Tschudi, M., Appel, I., Maslanik, J., Baldwin, D., Wang, X., Meade, P.:
781 Snow and ice products from Suomi NPP VIIRS, *J. Geophys. Res.: Atmos.*, 118, 12816–12830, 2013.
- 782 Kikuchi, K., Kameda, T., Higuchi, K., and Yamashita, A.: A global classification of snow crystals, ice crystals, and
783 solid precipitation based on observations from middle latitudes to polar regions, *Atmos. Res.*, 132–133, 460–472,
784 2013.
- 785 Kim, E., Gatebe, C., Hall, D., Newlin, J., Misakonis, A., Elder, K., Marshall, H., Hiemstra, C., Brucker, L., De
786 Marco, E., Crawford, C., Kang, D., H., Entin, J.: NASA’s SnowEx campaign: Observing seasonal snow in a forested
787 environment, *2017 IEEE International Geoscience and Remote Sensing Symposium (IGARSS)*,
788 DOI: 10.1109/IGARSS.2017.8127222, 2017.
- 789 King, M.D., Platnick, S., Menzel, W.P., Ackerman, S.A., Hubanks, P.A.: Spatial and temporal distribution of clouds
790 observed by MODIS onboard the Terra and Aqua satellites, *IEEE Trans. Geosci. Remote Sens.* 51 (7), 3826–3852,
791 2013.
- 792 Klein, A.G. and Stroeve, J.: Development and validation of a snow albedo algorithm for the MODIS
793 instrument, *Annals of Glaciology*, 34:45–52, 2002
- 794 Kokhanovsky, A. A. and Zege, E. P.: Scattering optics of snow, *Appl. Optics*, 43, 1589–1602, 2004
- 795 Kokhanovsky, A., Lamare, M., Di Mauro, B., Picard, G., Arnaud, L., Dumont, M., Tuzet, F., Brockmann, C., and
796 Box, J. E.: On the reflectance spectroscopy of snow, *The Cryosphere*, 12, 2371–2382, [https://doi.org/10.5194/tc-12-](https://doi.org/10.5194/tc-12-2371-2018)
797 [2371-2018](https://doi.org/10.5194/tc-12-2371-2018), 2018.
- 798 Kokhanovsky, A., Lamare, M.; Danne, O., Brockmann, C., Dumont, M., Picard, G., Arnaud, L., Favier, V., Jourdain,
799 B.; Le Meur, E., Di Mauro, B., Aoki, T., Niwano, M., Rozanov, V., Korkin, S., Kipfstuhl, S., Freitag, J., Hoerhold,
800 M., Zuhr, A., Vladimirova, D., Faber, A.-K., Steen-Larsen, H.C., Wahl, S., Andersen, J.K., Vandecrux, B., van As,
801 D., Mankoff, K.D., Kern, M., Zege, E., Box, J.E.: Retrieval of Snow Properties from the Sentinel-3 Ocean and Land
802 Colour Instrument, *Remote Sens.*, 11, 2280, 2019.
- 803 Koren, I., Remer, L., Kaufman, Y. J., Rudich, Y., and Martins, J.: On the twilight zone between clouds and aerosols,
804 *Geophys. Res. Lett.*, 34(8), L08805, doi:10.1029/2007GL029253, 2007.
- 805 LaChapelle, E. R.: Field Guide to Snow Crystals. University of Washington Press, 112 pp, 1969.



- 806 Lawson, P., Baker, B., Zmarzly, P., O'Connor, D., Mo, Q., Gayet, J.-F., and Shcherbakov, V.: Microphysical and
807 optical properties of ice crystals at South Pole Station, *J. Appl. Meteor. Climatol.*, 45(11), 1505–1524,
808 doi:10.1175/JAM2421.1, 2006.
- 809 Leroux C., and Fily M. : Modeling the effect of sastrugi on snow reflectance, *J. Geophys. Res.*, 103, 25,779-
810 25,788, 1998.
- 811 Liu X. and Yanai M.: Influence of Eurasian spring snow cover on Asian summer rainfall, *International Journal of*
812 *Climatology*, 22 (9), 1075-1089, <https://doi.org/10.1002/joc.784>,2002.
- 813 Liston, G. E., and C. A. Hiemstra: The Changing Cryosphere: Pan-Arctic Snow Trends (1979–2009). *J. Climate*, 24,
814 5691–5712, <https://doi.org/10.1175/JCLI-D-11-00081.1>, 2011
- 815 Lemke, P., J. Ren, R.B. Alley, I. Allison, J. Carrasco, G. Flato, Y. Fujii, G. Kaser, P. Mote, R.H. Thomas and T.
816 Zhang: Observations: Changes in Snow, Ice and Frozen Ground. In: *Climate Change 2007: The Physical Science*
817 *Basis. Contribution of Working Group I to the Fourth Assessment Report of the Intergovernmental Panel on Climate*
818 *Change* [Solomon, S., D. Qin, M. Manning, Z. Chen, M. Marquis, K.B. Averyt, M. Tignor and H.L. Miller (eds.)].
819 Cambridge University Press, Cambridge, United Kingdom and New York, NY, USA, 2007
- 820 Li, W., Stamnes, K., Chen, B., and Xiong, X.: Snow grain size retrieved from near-infrared radiances at multiple
821 wavelengths, *Geophys. Res. Lett.*, 28, 1699–1702, doi:10.1029/2000GL011641, 2001.
- 822 Lyapustin, A. I.: Atmospheric and geometrical effects on land surface albedo. *Journal of Geophysical Research:*
823 *Atmospheres*, 104(D4), 4127–4143. doi:10.1029/1998jd200064, 1999.
- 824 Lyapustin, A., Tedesco, M., Wang, Y.J., Aoki, T., Hori, M. and Kokhanovsky, A. : Retrieval of snow grain size over
825 Greenland from MODIS, *Remote Sensing of Environment*, 113, 1976-1987,2009.
- 826 Lyapustin, A., Wang, Y., Xiong, X., Meister, G., Platnick, S., Levy, R., Franz, B., Korin, S., Hilker, T., Tucker, J.,
827 Hall, F., Sellers, P., Wu, A., and Angal, A.: Scientific impact of MODIS C5 calibration degradation and C6+
828 improvements, *Atmos. Meas. Tech.*, 7, 4353-4365, <https://doi.org/10.5194/amt-7-4353-2014>, 2014.
- 829 Macke, A., Mueller, J., and Raschke, E.: Single scattering properties of atmospheric ice crystals, *J. Atmos. Sci.*, 53,
830 2813–2825, 1996.



- 831 Mary, A., Dumont, M., Dedieu, J.-P., Durand, Y., Sirguey, P., Milhem, H., Mestre, O., Negi, H. S., Kokhanovsky,
832 A. A., Lafayssse, M., and Morin, S.: Intercomparison of retrieval algorithms for the specific surface area of snow
833 from near-infrared satellite data in mountainous terrain, and comparison with the output of a semi-distributed
834 snowpack model, *The Cryosphere*, 7, 741–761, <https://doi.org/10.5194/tc-7-741-2013>, 2013.
- 835 McFarlane, S. A., Marchand, R. T., and Ackerman, T. P.: Retrieval of cloud phase and crystal habit from Multiangle
836 Imaging Spectroradiometer (MISR) and Moderate Resolution Imaging Spectroradiometer (MODIS) data, *J.*
837 *Geophys. Res.-Atmos.*, 110, D14201, doi:10.1029/2004JD004831, 2005.
- 838 Mei, L. L., Rozanov, V., Vountas, M., Burrows, J., Levy, R., Lotz, W.: A Cloud masking algorithm for the XBAER
839 aerosol retrieval using MERIS data. *Remote Sensing of Environment*. 197, 141-160,
840 <http://dx.doi.org/10.1016/j.rse.2016.11.016>, 2017.
- 841 Mei, L.L., Rozanov, V., Vountas, M., Burrows, J.P.: The retrieval of ice cloud parameters from multi-spectral
842 satellite observations of reflectance using a modified XBAER algorithm. *Remote Sensing of Environment*.
843 215(15),128-144,2018.
- 844 Mei, L., Vandenbussche, S., Rozanov, V., Proestakis, E., Amiridis, V., Callewaert, S., Vountas, M., Burrows, J. P.,
845 2020, On the retrieval of aerosol optical depth over cryosphere using passive remote sensing, *Remote Sensing of*
846 *Environment*, 241, 111731, <https://doi.org/10.1016/j.rse.2020.111731>, 2020a.
- 847 Mei, L.L., Rozanov, V., Ritter, C., Heinold, B., Jiao, Z.T., Vountas, M., Burrows, J.P.: Retrieval of aerosol optical
848 thickness in the Arctic snow-covered regions using passive remote sensing: impact of aerosol typing and surface
849 reflection model. *IEEE Transactions on Geoscience and Remote Sensing*. 10.1109/TGRS.2020.2972339, 1-15.
850 2020b.
- 851 Mei, L., Rozanov, V. and Burrows, J. P., : A fast and accurate radiative transfer model for aerosol remote
852 sensing, *Journal of Quantitative Spectroscopy and Radiative Transfer*, 256,107270, 2020c
- 853 Mei, L., Rozanov, V., Pohl, C., Vountas, M. and Burrows, J. P.: The retrieval of snow properties from SLSTR/
854 Sentinel-3 - part 1: method description and sensitivity study, *The Cryosphere*, 2020d



- 855 Nakamura, T., O. Abe, T. Hasegawa, R. Tamura, and T. Ohta: Spectral reflectance of snow with a known particle-
856 size distribution in successive metamorphism. *Cold Reg. Sci. Technol.*, 32, 13–26, [https://doi.org/10.1016/S0165-](https://doi.org/10.1016/S0165-232X(01)00019-2)
857 232X(01)00019-2, 2001.
- 858 Nakaya, U., Sekido, Y., General classification of snow crystals and their frequency of occurrence. *J. Fac. Sci.*,
859 Hokkaido Imperial Univ., Ser. II I-9, 234–264, 1938
- 860 Nakoudi, K.; Ritter, C.; Böckmann, C.; Kunkel, D.; Eppers, O.; Rozanov, V.; Mei, L.; Pefanis, V.; Jäkel, E.; Herber,
861 A.; Maturilli, M.; Neuber, R. Does the Intra-Arctic Modification of Long-Range Transported Aerosol Affect the
862 Local Radiative Budget? (A Case Study). *Remote Sens.*, 12, 2112, 2020.
- 863 Negi, H.S. and Kokhanovsky, A.: Retrieval of snow albedo and grain size using reflectance measurements in
864 Himalayan basin, *The Cryosphere*, 5, 203-217, 2011.
- 865 Painter, T. H., Dozier, J., Roberts, D. A., Davis, R. E., and Greene, R. O.: Retrieval of subpixel snow-covered area
866 and grain size from imaging spectrometer data, *Remote Sens. Environ.*, 85, 64– 77, 2003.
- 867 Painter, T.H., Rittger, K., McKenzie, C., Slaughter, P., Davis, R.E., Dozier, J.: Retrieval of subpixel snow covered
868 areas, grain size, and albedo from MODIS, *Remote Sensing of Environment*, 113, 868-879, 2009.
- 869 Pirazzini, R., Räisänen, P., Vihma, T., Johansson, M., and Tastula, E.-M.: Measurements and modelling of snow
870 particle size and shortwave infrared albedo over a melting Antarctic ice sheet, *The Cryosphere*, 9, 2357-2381,
871 <https://doi.org/10.5194/tc-9-2357-2015>, 2015.
- 872 Pohl C., Rozanov V.V. , Mei L. , Burrows J.P., Heygster G. and Spreen G.: Implementation of an ice crystal single-
873 scattering property database in the radiative transfer model SCIATRAN, *J. Quant. Spectrosc. Radiat. Transfer*,
874 doi: <https://doi.org/10.1016/j.jqsrt.2020.107118>, 2020
- 875 Popp, T., de Leeuw, G., Bingen, C., Bruhl, C., Capelle, V., Chedin, A., Clarisse, L., Dubovik, O., Grainger, R.,
876 Griesfeller, J., Heckel, A., Kinne, S., Kluser, L., Kosmale, M., Kolmonen, P., Lelli, L., Litvinov, P., Mei, L., North,
877 P., Pinnock, S., Povey, A., Robert, C., Schulz, M., Sogacheva, L., Stebel, K., Stein Zweers, D., Thomas, G., Tilstra,
878 L. G., Vandenbussche, S., Veeffkind, P., Vountas, M., and Xue, Y.: Development, Production and Evaluation of
879 Aerosol Climate Data Records from European Satellite Observations (Aerosol_cci), *Remote Sensing*, 8, 421,
880 doi:10.3390/rs8050421, <http://www.mdpi.com/2072-4292/8/5/421>, 2016.



- 881 Räisänen, P., Makkonen, R., Kirkevåg, A., and Debernard, J. B.: Effects of snow grain shape on climate simulations:
882 sensitivity tests with the Norwegian Earth System Model, *The Cryosphere*, 11, 2919-2942,
883 <https://doi.org/10.5194/tc-11-2919-2017>, 2017.
- 884 Rittger, K., Painter, T. H. and Dozier, J.: Assessment of methods for mapping snow cover from MODIS, *Advances*
885 *in Water Resources*, 51(35th Year Anniversary Issue), 367–380. doi:10.1016/j.advwatres.2012.03.002, 2013.
- 886 Rozanov, V. V., Rozanov, A. V., Kokhanovsky, A. A., and Burrows, J. P.: Radiative transfer through terrestrial
887 atmosphere and ocean: Software package SCIATRAN, *J. Quant. Spect. Rad. Trans.* 133, 13–71, doi:10.5194/acp-
888 8-1963-2008, 2014.
- 889 Rutter, N., J. Pan, M. Durand, J. King, C. Derksen, and F. Larue. : *SnowEx17 Laser Snow Microstructure Specific*
890 *Surface Area Data, Version 1*. [Indicate subset used]. Boulder, Colorado USA. NASA National Snow and Ice Data
891 Center Distributed Active Archive Center. doi: <https://doi.org/10.5067/H9C1UVWN1UK3>, 2018.
- 892 Ryan, J. C., Smith, L. C., van As, D., Cooley, S. W., Cooper, M. G., Pitcher, L. H., and Hubbard, A.: Greenland Ice
893 Sheet surface melt amplified by snowline migration and bare ice exposure, *Science Advances*, 5,
894 <https://doi.org/10.1126/sciadv.aav3738>, <http://advances.sciencemag.org/content/5/3/eaav3738>, 2019.
- 895 Saito, M., P. Yang, N. G. Loeb, and S. Kato: A novel parameterization of snow albedo based on a two-layer snow
896 model with a mixture of grain habits, *J. Atmos. Sci.*, 76, 1419–1436, 2019.
- 897 Sarangi, C., Qian, Y., Rittger, K., Bormann, K. J., Liu, Y., Wang, H., Wan, H., Lin, G., and Painter, T. H.: Impact
898 of light-absorbing particles on snow albedo darkening and associated radiative forcing over high-mountain Asia:
899 high-resolution WRF-Chem modeling and new satellite observations, *Atmos. Chem. Phys.*, 19, 7105–7128,
900 <https://doi.org/10.5194/acp-19-7105-2019>, 2019.
- 901 Sokratov, S. and Kazakov, N.: Dry snow metamorphism expressed by crystal shape, *Ann. Glaciol.*, 2012,
902 vol. 58 (61), 51–56, 2012.
- 903 Stamnes, K., Li, W., Eide, H., Aoki, T., Hori, M. and Storvold, R.: ADEOSII/GLI snow/ice products - part I:
904 Scientific basis, *Remote Sens. Environ.*, 111, 258–273, doi:10.1016/j.rse.2007.03.023, 2007.



- 905 Tanikawa T., Kuchiki K., Aoki T., Ishimoto H., Hachikubo A., Niwano M., Hosaka M.,
906 Matoba S., Kodama Y., Iwata Y., and Stamnes K.: Effects of snow grain shape and mixing state of
907 snow impurity on retrieval of snow physical parameters from ground - based optical instrument, *Journal of*
908 *Geophysical Research: Atmospheres*, <https://doi.org/10.1029/2019JD031858>, 2020
- 909 Thackeray, C. W., & Fletcher, C. G.: Snow albedo feedback Current knowledge, importance, outstanding issues
910 and future directions. *Progress in Physical Geography*, 40(3), 392–408. doi:10.1177/0309133315620999, 2016.
- 911 Wiebe, H., Heygster, G., Zege, E., Aoki, T., and Hori, M.: Snow grain size retrieval SGSP from optical satellite data:
912 Validation with ground measurements and detection of snow fall events, *Remote Sens. Environ.*, 128, 11–20,
913 <https://doi.org/10.1016/j.rse.2012.09.007>, 2013.
- 914 Wendisch, M., Muller, D., Schell, D., and Heintzenberg, J.: An air- borne spectral albedometer with active
915 horizontal stabilization, *J. Atmos. Oceanic Technol.*, 18, 1856–1866, 2001
- 916 Wendisch, M., Pilewskie, P., Jakel, E., Schmidt, S., Pommier, J., Howard, S., Jonsson, H. H., Guan, H., Schroder,
917 M., and Mayer, B.: Airborne measurements of areal spectral surface albedo over different sea and land surfaces, *J.*
918 *Geophys. Res.*, 109, D08203, doi:10.1029/2003JD004392, 2004.
- 919 Xiong, C., & Shi, J.: Snow specific surface area remote sensing retrieval using a microstructure based reflectance
920 model. *Remote Sensing of Environment*, 204, 838–849. doi:10.1016/j.rse.2017.09.017, 2018
- 921 Yang, P., Bi, L., Baum, B. A., Liou, K.-N., Kattawar, G. W., Mishchenko, M. I. And Cole, B.: Spectrally consistent
922 scattering, absorption, and polarization properties of atmospheric ice crystals at wavelengths from 0.2 to 100 μm , *J.*
923 *Atmos. Sci.*, 70, 330–347, 2013.
- 924 Zege, E. P., Kokhanovsky, A. A., Katsev, I. L., Polonsky, I. N., and Prikhach, A. S.: The retrieval of the effective
925 radius of snow grains and control of snow pollution with GLI data. In M. I. Hovenier (Ed.), Proceedings of
926 conference on light scattering by nonspherical particles: theory, measurements, and applications (pp. 288–290).
927 Boston, Mass: *American Meteorological Society*, 1998.
- 928 Zege, E.P., Katsev, I.L., Malinka, A.V., Prikhach, A.S., Heygster, G. and Wiebe H.: Algorithm for retrieval of the
929 effective snow grain size and pollution amount from satellite measurements, *Remote sensing of Environment*, 115,
930 2674-2685, 2011.



- 931 Zhang, T., Wang T., Krinner G., Wang, X., Gasser, T., Peng S., Piao S. and Yao T.: The weakening relationship
932 between Eurasian spring snow cover and Indian summer monsoon rainfall. *Science advances*, 5(3), DOI:
933 10.1126/sciadv.aau8932, 2019.
- 934 Zhao, S., Jiang, T., Wang, Z.: Snow grain-size estimation using Hyperion imagery in a typical area of the Heihe
935 river basin, China. *Remote Sens.*, 5, 238–253, 2013.